Journal of Colloid and Interface Science 556 (2019) 335–344

Contents lists available at ScienceDirect

Journal of Colloid and Interface Science

journal homepage: www.elsevier.com/locate/jcis

Regular Article

In situ construction of WO_3 nanoparticles decorated Bi_2MoO_6 microspheres for boosting photocatalytic degradation of refractory pollutants

Shijie Li [a], Shiwei Hu [a], Wei Jiang [a], Junlei Zhang [b], Kaibing Xu [c,*], Zhaohui Wang [d,e,*]

[a] Key Laboratory of Key Technical Factors in Zhejiang Seafood Health Hazards, Institute of Innovation & Application, Zhejiang Ocean University, Zhoushan, Zhejiang Province 316022, China
[b] Department of Environmental Science and Engineering, Fudan University, Shanghai 200433, China
[c] State Key Laboratory for Modification of Chemical Fibers and Polymer Materials, Research Center for Analysis and Measurement, Donghua University, Shanghai 201620, China
[d] Shanghai Key Laboratory of Urbanization and Ecological Restoration, School of Ecological and Environmental Sciences, East China Normal University, Shanghai 200241, China
[e] Institute of Eco-Chongming (IEC), Shanghai 200062, China

GRAPHICAL ABSTRACT

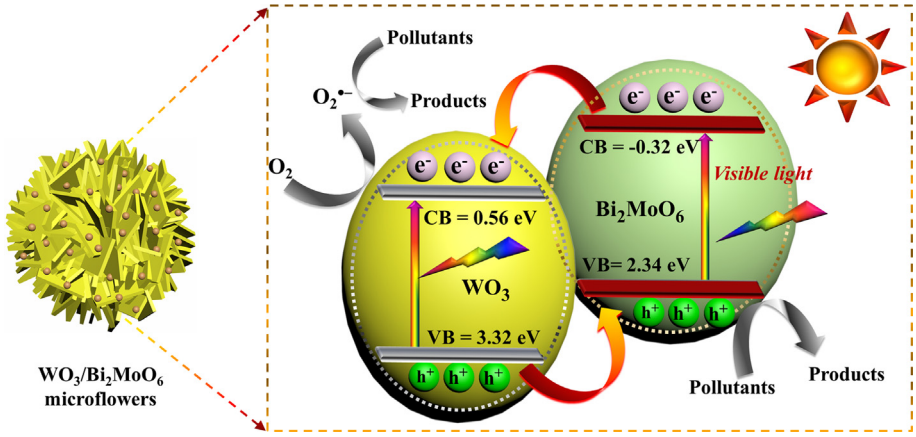

ARTICLE INFO

Article history:
Received 22 June 2019
Revised 21 August 2019
Accepted 21 August 2019
Available online 22 August 2019

Keywords:
WO_3/Bi_2MoO_6
Heterojunction
Electrospinning
Visible-light photocatalysis

ABSTRACT

Visible-light-driven (VLD) heterojunction photocatalysts for refractory contaminant degradation have aroused huge interest because of their outstanding photocatalytic performance. From the aspect of practical application, it is important to develop a highly efficient, durable, eco-friendly and inexpensive VLD photocatalyst. Herein, we report a novel VLD WO_3/Bi_2MoO_6 heterojunction photocatalyst with remarkable photocatalytic activity, which was fabricated via an electrospinning–calcination–solvothermal route. The phase, composition, morphologies, and optical properties of WO_3/Bi_2MoO_6 heterojunctions were comprehensively characterized. The photocatalytic performance of WO_3/Bi_2MoO_6 heterojunctions was assessed by the removal of rhodamine (RhB) and tetracycline hydrochloride (TC) under visible light (VL). WO_3/Bi_2MoO_6 heterojunctions displayed superior photocatalytic activities compared to Bi_2MoO_6, WO_3, or the mechanical mixture of WO_3 and Bi_2MoO_6. In particular, the heterojunction material (0.4WB, theoretical molar ratio of WO_3/Bi_2MoO_6 is 0.4/1.0) exhibited the best degradation efficiency (100%) and mineralization rate (52.3%) in 90 min, both of which exceeded the observed rates for Bi_2MoO_6 by 5.3 and 6.4 times, respectively. Moreover, 0.4WB showed a good durability in eight runs.

* Corresponding authors.
E-mail addresses: xukaibing@dhu.edu.cn (K. Xu), zhwang@des.ecnu.edu.cn (Z. Wang).

https://doi.org/10.1016/j.jcis.2019.08.077

The optimized photocatalytic property of WO_3/Bi_2MoO_6 can be attributed to enhanced VL absorption and reduced recombination efficiency of carriers owing to the synergistic effects between Bi_2MoO_6 and WO_3. The necessity of direct contact between WO_3/Bi_2MoO_6 and contaminants was experimentally verified. The study on photocatalytic mechanism demonstrates that superoxide free radicals (O_2^-) and photogenerated hole (h^+) are dominantly responsible for the pollutant degradation, as demonstrated by the trapping experiments and electron spin resonance (ESR) analysis. Therefore, the WO_3/Bi_2MoO_6 heterojunction holds huge potential to be utilized as a durable and highly active photocatalyst for wastewater treatment.

1. Introduction

Water pollution is becoming severe due to the increasing discharge of toxic and refractory organic contaminants into aqueous environments, such as antibiotics, industrial dyes, pesticides, and pharmaceutical compounds, *etc.* [1]. Facing the enormous challenge of environmental deterioration, it is essential to develop an eco-friendly technology to restore environment [2,3]. Semiconductor photocatalysis technique that can utilize inexhaustible solar energy to efficiently degrade and even mineralize hazardous pollutants thoroughly has huge potential in resolving environmental problems [4–11]. To realize this goal, the core issue is to explore highly active and durable photocatalysts with sufficient sunlight absorption and high charge separation rate [1,12–16]. As one of the simplest Aurivillius phase compound, Bi_2MoO_6, built from $[Bi_2O_2]^{2+}$ slices connecting with MoO_6 octahedron, has been the hotspot in the field of environmental remediation owing to its VL response, excellent stability, low cost, and nontoxicity [17]. However, serious recombination of photo-induced charge carriers and limited VL response range are still two primary drawbacks that restrain its photocatalytic performance [18–20]. Therefore, several methods including morphology engineering [21], noble metal deposition [22], doping/defect-introduction [23,24], and heterojunction fabrication [25–31], have been employed to resolve such problems for improving the photocatalytic property of Bi_2MoO_6. Among these strategies, heterojunction construction has been demonstrated to be a feasible and effective route [32]. As a result, a variety of Bi_2MoO_6-based heterojunctions exhibiting intense optical absorption and high photocatalytic activity, have been constructed [25–31]. Although some advances have been achieved, further rational design of novel Bi_2MoO_6-based heterojunctions with outstanding photocatalytic performance for environmental pollution control is still required for both scientific research and practical applications.

WO_3 with a medium band gap (2.4–2.8 eV) is reported as a promising semiconductor by virtue of its strong VL absorption, non-toxicity, strong oxidizing capability of valence holes and good stability [33–37]. More importantly, the well aligned straddling band structures that can accelerate the charge transfer and reduce the recombination of photo-excited carriers, can be established between WO_3 and Bi_2MoO_6. Considering these merits, it is highly desirable to fabricate WO_3/Bi_2MoO_6 heterojunctions and examine their capability for degrading refractory pollutants via VL photocatalysis.

Herein, hierarchical WO_3/Bi_2MoO_6 heterojunctions were prepared via a facile procedure and then used for efficient photodegradation of toxic pollutants under VL. It was verified that the strong interactions between WO_3 and Bi_2MoO_6 pronouncedly optimize the light harvesting ability and boost the separation and transfer of photogenerated carriers. Such an improvement rendered WO_3/Bi_2MoO_6 heterojunctions a markedly upgraded photocatalytic performance in decomposing toxic pollutants. These results provide a novel and facile route for the construction of Bi_2MoO_6-based heterojunctions in wastewater purification.

2. Experiment

2.1. Chemicals

Ethylene glycol (EG, >99%), *N,N*-dimethyformamide (DMF, >98%), tungsten chloride (WCl_6, >98%), bismuth nitrate pentahydrate ($Bi(NO_3)_3{\cdot}5H_2O$, >99%), polyvinylpyrrolidone (PVP, Mw = 1 300 000), ammonium oxalate (AO, >99%), tetracycline hydrochloride (TC, >99%), *p*-benzoquinone (BQ, >98%), rhodamine B (RhB, >99%), sodium molybdate dihydrate ($Na_2MoO_4{\cdot}2H_2O$, >98%), and isopropanol (IPA, >98%) were purchased from Chinese Sinopharm.

2.2. Photocatalysts preparation

WO_3 was fabricated by an electrospinning route (Fig. 1). Typically, 1.6 g of WCl_6 and 1.9 g of PVP were sequentially dissolved in 11 mL DMF with the assistance of magnetically stirring. After vigorous agitation for 24 h the homogeneous solution of WCl_6, PVP, and DMF was obtained for electrospinning. A voltage of 14 kV was applied. Subsequently, the as-prepared nanofibers were put in a muffle furnace and annealed at 500 °C for 2 h in air to obtain the WO_3 product.

WO_3/Bi_2MoO_6 heterojunctions were constructed via a solvothermal route (Fig. 1). Briefly, 1 mmol $Bi(NO_3)_3{\cdot}5H_2O$ and 0.5 mmol $Na_2MoO_4{\cdot}2H_2O$ were sequentially dissolved in 40 mL of ethylene glycol. Then the WO_3 nanofibers (0.2, 0.4 or 0.6 mmol) were ultrasonically dispersed in the above solution for 0.5 h and then blended with 40 mL of ethanol, followed by vigorous agitation for 2 h. Finally, the solution was loaded into a 100 mL autoclave, followed by solvothermal treatment at 160 °C for 24 h. The as-obtained samples are separately named as 0.2WB, 0.4WB and 0.6WB.

2.3. Characterization

X-ray diffraction data of all the catalysts was collected by a Bruker D8 Advance diffractometer. The morphology was recorded by scanning electron microscopy (SEM, Hitachi S–4800) and transmission electron microscopy (HADDF STEM, Tecnai G2F20), and the elemental composition data was obtained by energy-disperse X-ray spectroscopy (EDS). XPS data was acquired by a spectrometer (Thermo SCIENTIFIC). Photoluminescence (PL) spectra were obtained by a fluorescence spectrophotometer (Hitachi F-7000). The UV–vis diffuse reflectance spectra (DRS) were detected by using a Cary 300 UV–vis spectrophotometer. Electron spin resonance (ESR) spectra of spin-trapping radicals by DMPO were recorded at room temperature on a Bruker ESR 300E spectrometer, operated under the following conditions: center field, 3510 G; sweep width, 100 G; microwave frequency, 9.87 GHz; microwave power, 18.75 mW.

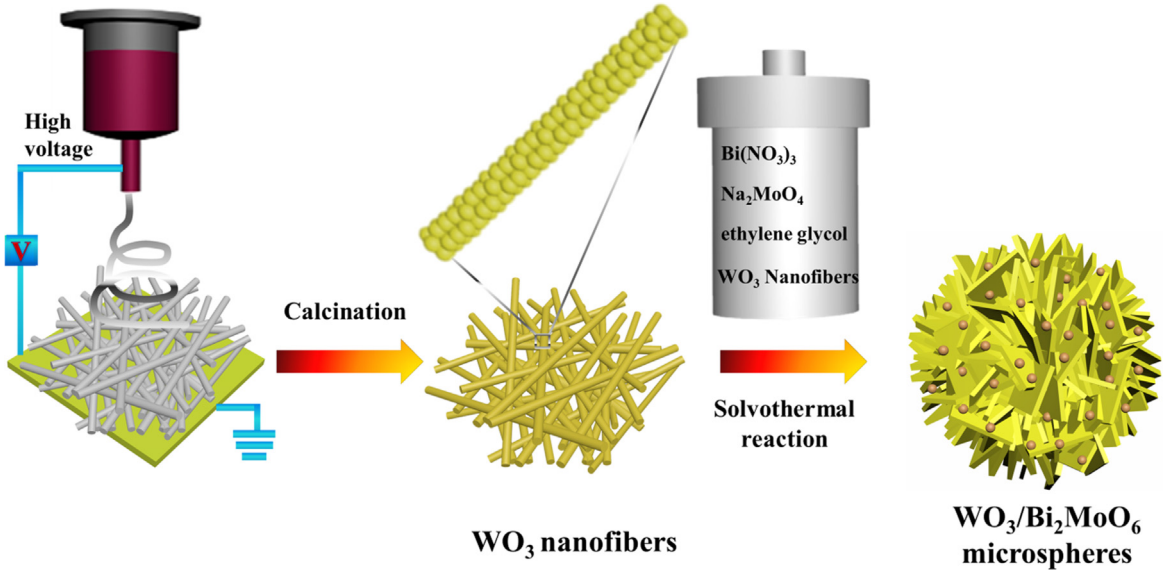

Fig. 1. Illustration of the preparation of WO_3/Bi_2MoO_6 heterojunctions.

2.4. Photocatalytic tests

The photocatalytic removal of RhB or TC was implemented under the light from a 300 W Xe lamp installed with a 400 nm cut-off filter. Specifically, the sample (50 mg) was suspended in RhB (20 mg/L, 100 mL), or TC (20 mg/L, 50 mL) aqueous solution. Prior to irradiation, the solution was vigorously agitated for 0.5 h in darkness to reach an adsorption/desorption equilibrium. Subsequently, the irradiation initiates the reaction. The concentration of RhB or TC was measured by the UV–vis spectrophotometer according to the characteristic peak for RhB at 554 nm or TC at 357 nm. Total organic carbon (TOC) values during photodegradation of RhB over various samples were detected to assess the mineralization ability of the catalysts.

3. Results and discussion

3.1. Structure and morphology

The crystalline phases of all samples were examined using XRD patterns. As illustrated in Fig. 2, bare Bi_2MoO_6 displays an orthorhombic phase (JCPDS 76-2388) with characteristic diffraction peaks at 28.4°, 32.2°, 46.3°, and 55.7°, in agreement with the (1 3 1), (0 0 2), (2 0 2) and (1 3 3) diffraction planes, respectively [19,38]. Pure WO_3 is crystallized in hexagonal phase (JCPDS 83-0951) with characteristic diffraction peaks at 23.2°, 23.7°, 24.3°, 33.3°, 34.2°, and 41.9°, corresponding to (0 0 2), (0 2 0), (2 0 0), (0 2 2), (2 0 2), and (2 2 2) diffraction planes, respectively [37]. The diffraction peaks of both Bi_2MoO_6 and WO_3 can be detected from the WO_3/Bi_2MoO_6 heterojunctions (0.2WB, 0.4WB and 0.6WB) without other detectable peaks, validating the high purity of these samples. Of note, the diffraction intensity of the WO_3 peaks gradually becomes stronger with the increase of WO_3 content.

The morphologies of the as-prepared Bi_2MoO_6, WO_3, and WO_3/Bi_2MoO_6 heterojunctions were studied by SEM and TEM. Pristine WO_3 prepared by an electrospinning-calcination procedure consists of numerous nanofibers (diameter: ~200 nm) (Fig. 3a). However, after solvothermal process, the WO_3 sample is composed of nanoparticles (diameter: about 20–50 nm) (Fig. 3b). The apparent evolution from nanofibers to nanoparticles should result from the breakage of the nanofibers into nanoparticles during the solvothermal reaction.

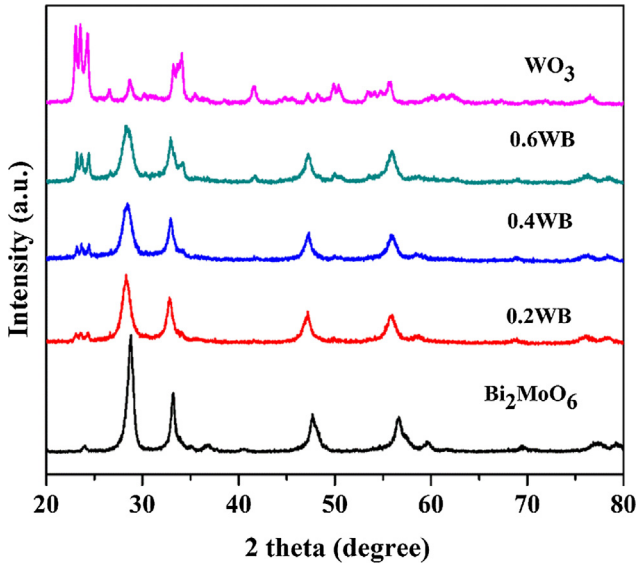

Fig. 2. XRD patterns of Bi_2MoO_6, WO_3, and WO_3/Bi_2MoO_6 heterojunctions (0.2WB, 0.4WB and 0.6WB).

Pristine Bi_2MoO_6 shows flowerlike nanostructures (diameter: 1.0–3.0 μm) (Fig. 4a) [31]. The in-situ formation of WO_3 on Bi_2MoO_6 exerts an impact on the nanostructure of the heterojunctions. With the increase of WO_3 content, WO_3/Bi_2MoO_6 heterojunction exhibits more irregular 3D hierarchical superstructure (Fig. 4b–d). Specifically, 0.4WB presents a micro-spherical superstructure with diameters in the range of ~0.8–2.5 μm (Fig. 4c), which is constructed by Bi_2MoO_6 nanosheets and WO_3 nanoparticles with a diameter of ~40 nm (Fig. 4e). Furthermore, the EDS spectra (Fig. 4f) show that W, Bi, Mo, and O elements coexist in 0.4WB, signifying that successful preparation of the WO_3/Bi_2MoO_6 heterojunction.

More morphological details on 0.4WB were further obtained using TEM images. Fig. 5a confirms the hierarchical superstructure of 0.4WB. Fig. 5b exhibits the corresponding high-resolution TEM

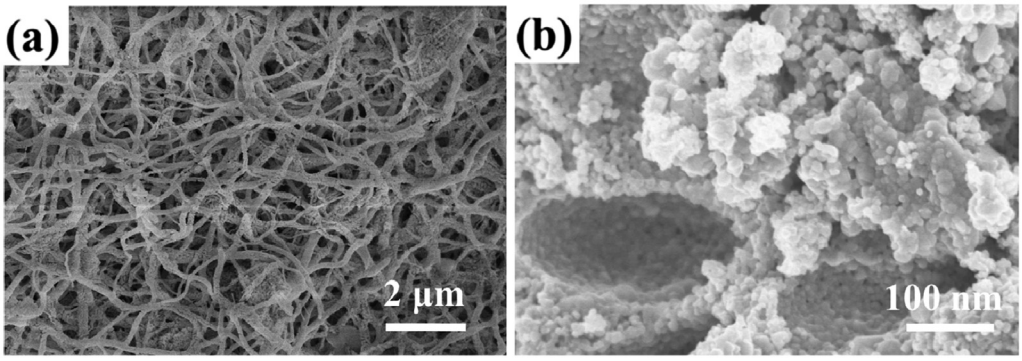

Fig. 3. SEM images of the as-prepared WO_3 (a) before and after solvothermal treatment (b).

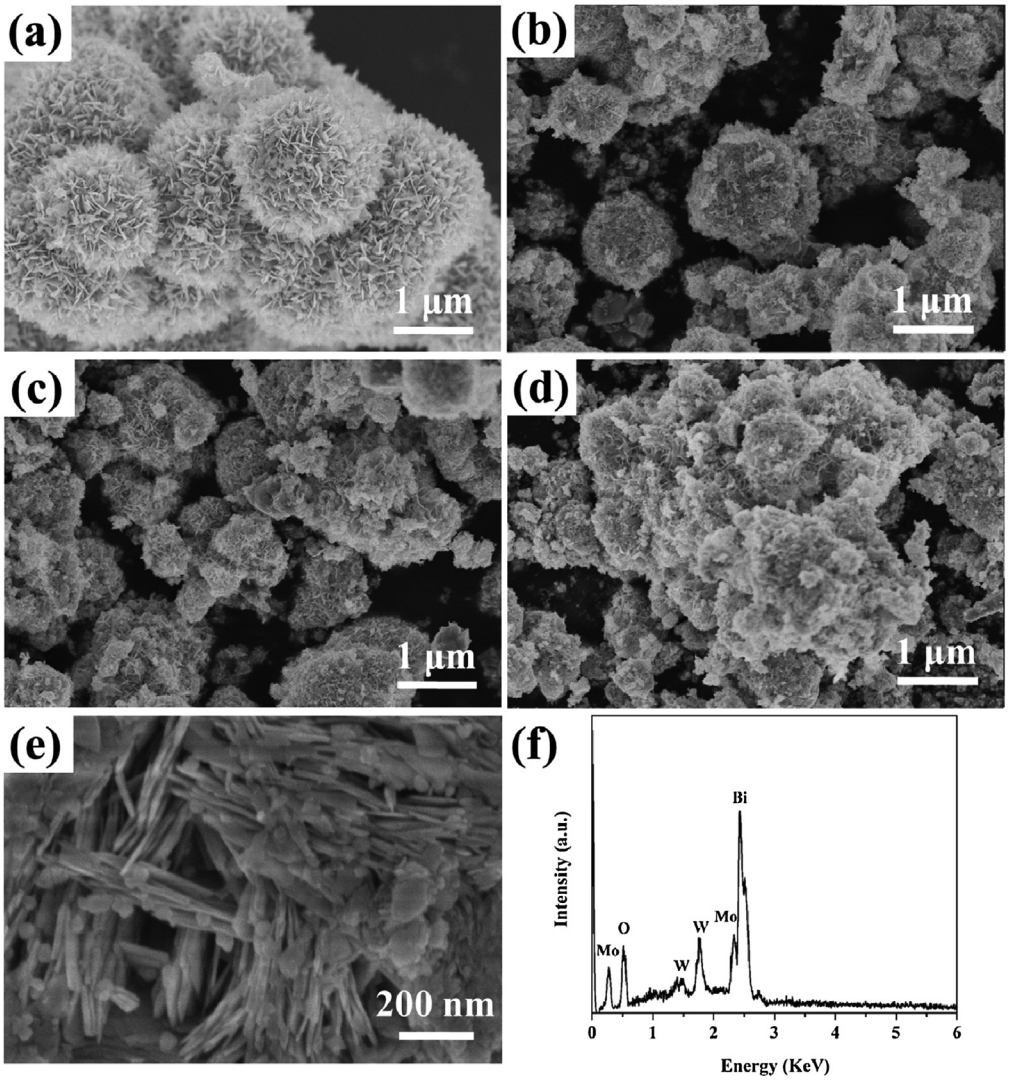

Fig. 4. SEM images of Bi_2MoO_6 (a), 0.2WB (b), 0.4WB (c, e), and 0.6WB (d); EDS spectrum of 0.4WB (f).

image of 0.4WB. The two adjacent lattice spacings of 0.37 nm and 0.33 nm at the interface agree with the Bi_2MoO_6 (1 1 1) plane [27] and the WO_3 (1 2 0) plane [34], respectively, indicating that WO_3 NPs are intimately attached to the Bi_2MoO_6 nanosheets. All these results demonstrate the successful fabrication of WO_3/Bi_2MoO_6 heterojunctions via the facile strategy.

3.2. Photoexcition properties

UV–Vis DRS was employed to illustrate the optical properties of Bi_2MoO_6, WO_3, and WO_3/Bi_2MoO_6 heterojunctions. As displayed in Fig. 6a, pristine Bi_2MoO_6 displays an absorption edge at ~466 nm [18], while pristine WO_3 exhibits an absorption edge at ~476 nm

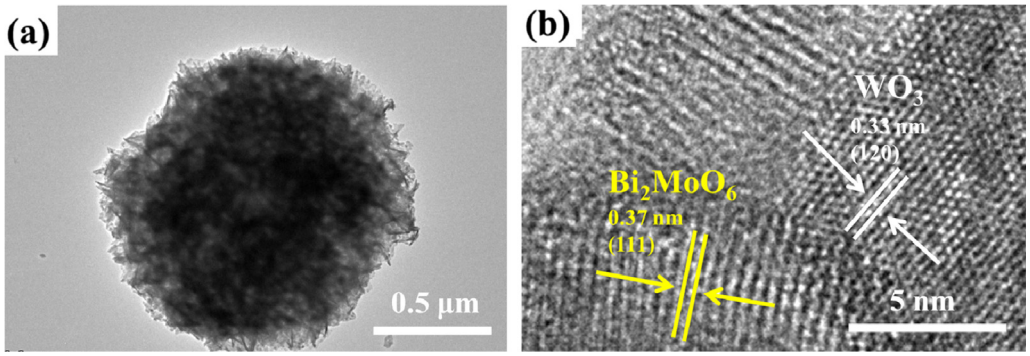

Fig. 5. (a, b) TEM images of 0.4WB.

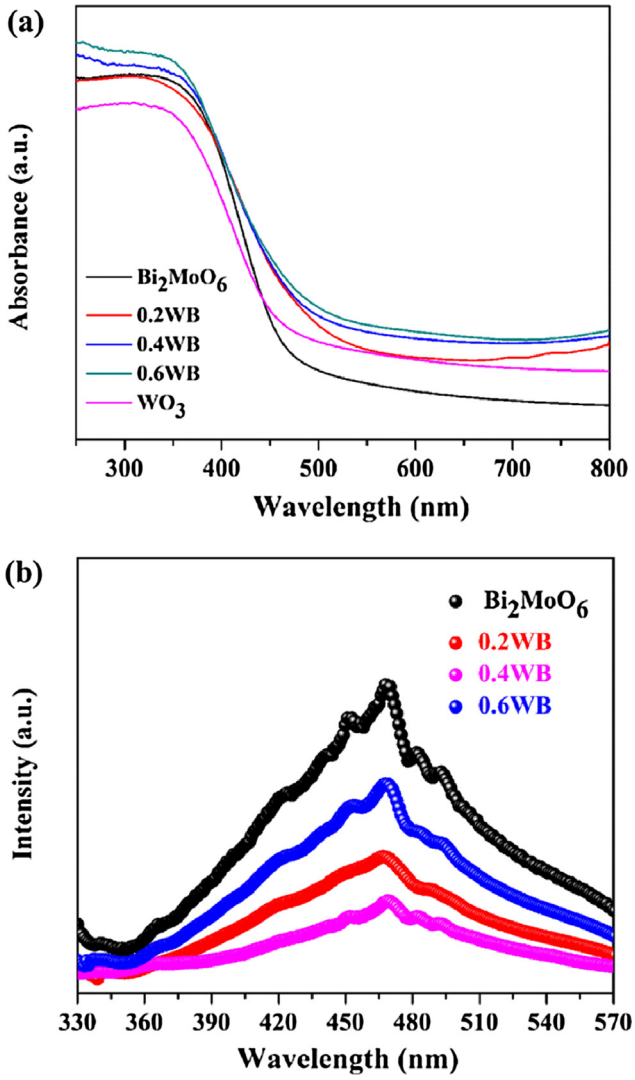

Fig. 6. (a) UV–Vis DRS of Bi_2MoO_6, WO_3, and WO_3/Bi_2MoO_6 heterojunctions (0.2WB, 0.4WB and 0.6WB); (b) PL spectra of Bi_2MoO_6 and WO_3/Bi_2MoO_6 heterojunctions.

[39]. Interestingly, the absorption in the VL region was enhanced and extended after Bi_2MoO_6 was modified by the WO_3, verifying that the WO_3/Bi_2MoO_6 heterojunctions could improve the utilization of sunlight and can possibly ameliorate the photocatalytic property toward pollutant degradation.

Photocatalysis primarily depends upon the separation and transfer rate of the photo-induced electron-hole pairs [29,35,40,41]. Since photoluminescence (PL) intensity can reflect the recombination efficiency of photo-excited carriers, the PL spectra of Bi_2MoO_6 and WO_3/Bi_2MoO_6 heterojunctions were recorded. In general, a stronger intensity represents a lower separation efficiency of charge carriers [36,42,43]. Fig. 6b exhibits the PL spectra of bare Bi_2MoO_6 and WO_3/Bi_2MoO_6 heterojunctions under the excitation wavelength of 300 nm. Pure Bi_2MoO_6 displays an intense emission peak located at ca. 370 nm, in agreement with the literature [31]. Comparatively, the PL intensity for WO_3/Bi_2MoO_6 heterojunctions is weakened dramatically, indicating the effective separation of charge carriers through the WO_3/Bi_2MoO_6 interface. Notably, 0.4WB shows the lowest PL intensity, which reveals the most effective separation of carriers and thereby implies the best photocatalytic performance.

3.3. Photocatalytic performance

The photocatalytic properties of WO_3/Bi_2MoO_6 heterojunctions for toxic pollutant degradation under VL were characterized. Fig. 7a shows the degradation profiles of RhB in different systems. As observed, no RhB was decomposed without catalysts after 90 min of VL illumination, indicating that RhB self-degradation can be ignored under present experimental conditions. The order of photocatalytic activity of the as-prepared samples can be summarized as follows: 0.4BW > 0.2BW > 0.6BW > Mixture > Bi_2MoO_6 > WO_3. These heterojunctions show markedly enhanced photocatalytic activity compared to pure Bi_2MoO_6 and WO_3. The excellent photocatalytic property of these heterojunctions gives credit to the fascinating hierarchical hetero-structure that enhances the VL harvesting capability (Fig. 6a) and largely promotes the separation of photo-induced carriers (Fig. 6b), thus greatly improving the photocatalytic performance. Specifically, 0.4BW shows the optimum activity, which can be explained by the fact that the most efficient separation of electrons and holes was found in 0.4BW, as verified by the weakest PL intensity of 0.4BW (Fig. 6b). Complete degradation of RhB by 0.4BW was reached within 90 min. For comparison, the mechanical mixture (86.8 wt% Bi_2MoO_6 + 13.2 wt% WO_3) was also employed to decompose RhB. However, only 23.9% of RhB was degraded, validating the establishment of closely contacted interface is beneficial to ameliorating the photocatalytic performance. Besides, the reaction kinetics of the RhB degradation process was calculated using the apparent first-order model (Fig. 7b). Remarkably, 0.4WB has the largest k value of 0.0393 min^{-1}, exceeding that of sole Bi_2MoO_6 (0.0022 min^{-1}), WO_3 (0.0015 min^{-1}), or the mixture (0.0030 min^{-1}) by approximately 17.8, 26.2, and 13.1 times, respectively.

To further confirm the photo-oxidation ability of 0.4BW, we also investigated the photocatalytic degradation of the TC

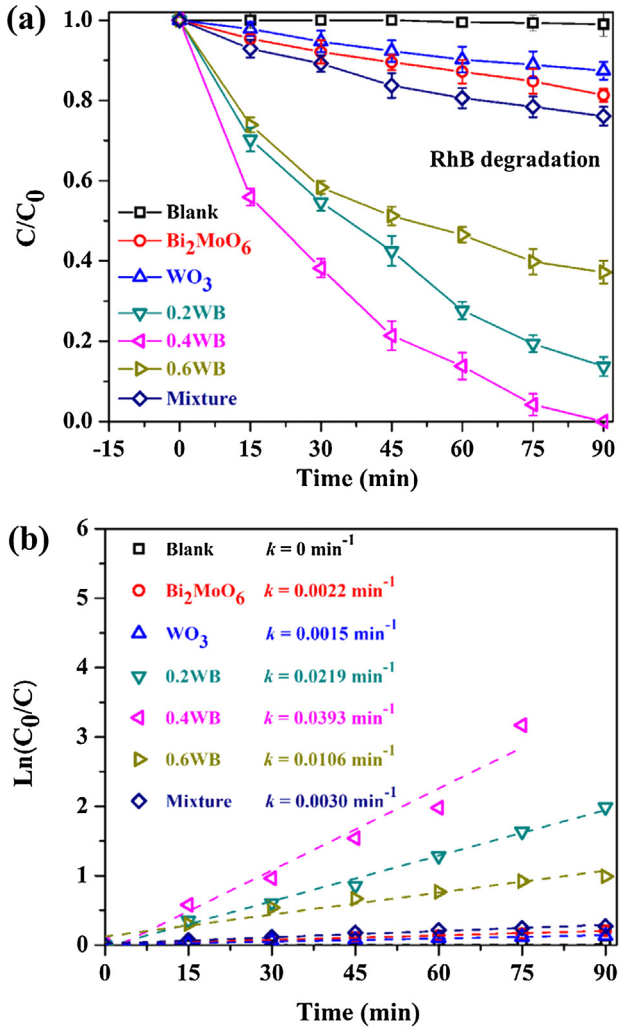

Fig. 7. Photocatalytic degradation of RhB (20 mg/L, 100 mL, pH = 6.3) using various catalysts (50 mg) under VL (a) and the corresponding degradation kinetics of RhB (b).

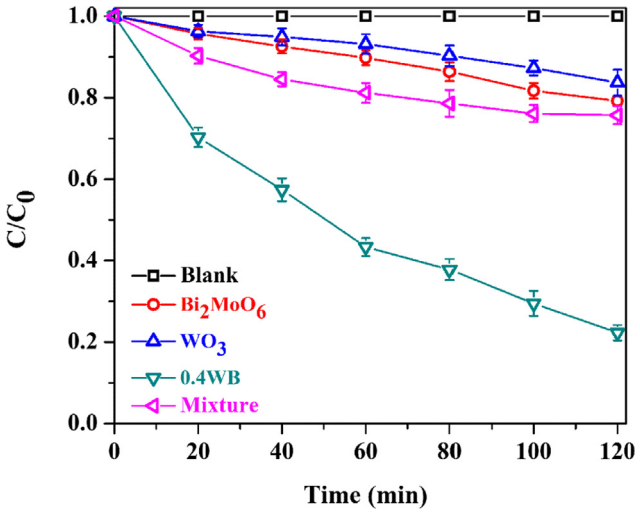

Fig. 8. Photocatalytic degradation of TC (20 mg/L, 50 mL, pH = 6.1) using Bi_2MoO_6 (50 mg), WO_3 (50 mg), 0.4WB (50 mg) and the mixture (43 mg Bi_2MoO_6 + 7 mg WO_3) under VL.

antibiotic, which could induce reproductive abnormalities to people. As demonstrated in Fig. 8, nearly 77.3% of TC was decomposed after treatment with 0.4BW for 120 min, while only 20.8%, 16.4%, and 24.3% of TC were decomposed by Bi_2MoO_6, WO_3, and the mixture, respectively. Analogous to RhB degradation, 0.4BW shows the most efficient photocatalytic degradation performance with the highest k value of 0.0119 min^{-1} that is about 5.3 and 7.5 folds higher than that of Bi_2MoO_6, and WO_3, respectively (Fig. S1). These findings validate the excellent photocatalytic properties of 0.4BW in the degradation of toxic pollutants.

The mineralization capability is also a crucial parameter to appraise the photocatalytic performance of photocatalysts. Thus, the mineralization degrees of RhB by Bi_2MoO_6, WO_3 and 0.4WB were examined by TOC. As displayed in Fig. 9a, the TOC removal ratios of RhB by using Bi_2MoO_6, WO_3 and 0.4WB reached 8.2%, 4.7% and 52.3% at 90 min, respectively, proving the superior photocatalytic mineralization capability of 0.4WB. The results demonstrate that 0.4WB can effectively mineralize RhB dye during the photocatalytic reaction, and further holds a promising potential for the practical application.

Equally importantly, ideal photocatalysts for the decomposition of toxic pollutants are not only required to possess excellent photocatalytic activity but also should be endowed with good stability

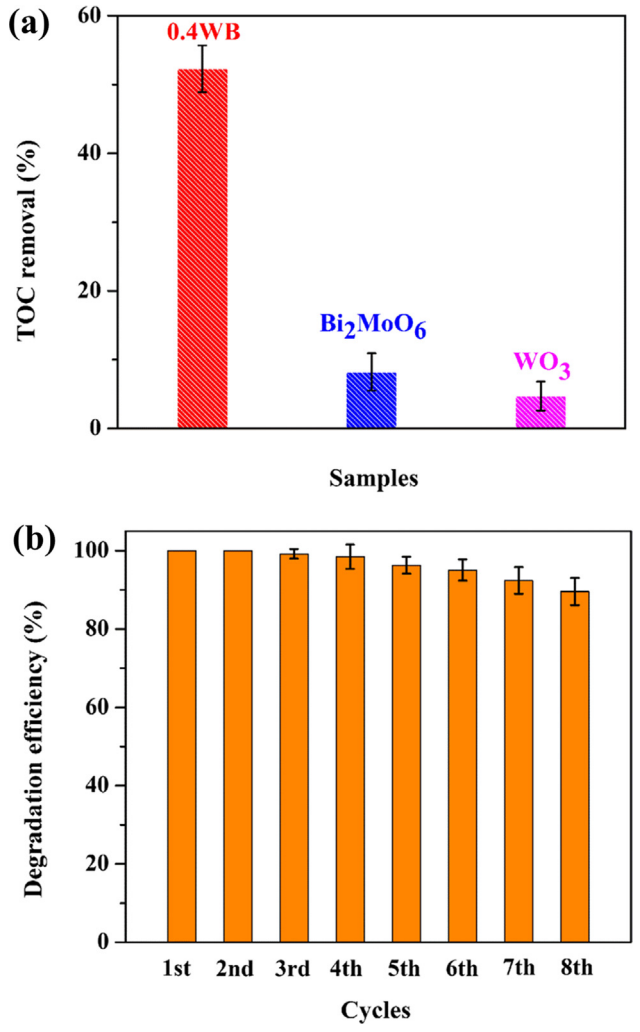

Fig. 9. (a) The TOC removal efficiency of RhB (20 mg/L, 100 mL, pH = 6.3) over Bi_2MoO_6 (50 mg), WO_3 (50 mg) and 0.4WB (50 mg) after 90 min of VL irradiation; (b) Cycling of 0.4WB (50 mg) sample for RhB (20 mg/L, 100 mL, pH = 6.3) removal.

for the practical application [44]. In this work, the reusability of WO_3/Bi_2MoO_6 was examined by conducting eight consecutive runs for the decomposition of RhB. As observed in Fig. 9b, 0.4 WB displays superior stability. The photocatalytic activity of 0.4WB declines slightly during the cycling tests. In addition, the crystal structure and nanostructure is sustained throughout the photodegradation process, as evidenced by the phase and morphology analysis on the catalyst after cycling runs (Figs. S2 and S3). The results demonstrate the good stability and reusability of 0.4WB.

3.4. Reaction mechanism

The photo-excited reactive oxygen species (ROS) produced during the 0.4BW photocatalytic process under VL illumination were firstly identified by the electron spin resonance (ESR) spectrum (Fig. 10a and b) [45]. DMPO was used as the spin-trap reagent in aqueous solution for ·OH and in methanolic solution for $O_2^{\cdot-}$, respectively, because the facile disproportionation of the superoxide species in water interferes with the spin trapping. No DMPO-O_2H spin adduct was detected in the dark in the presence of 0.4BW. Upon laser irradiation (λ = 532 nm), the characteristic sextet peaks of DMPO-O_2H adduct (in methanol solution) were observed (Fig. 10a). The identity of superoxide was further confirmed by the simulated hyperfine splitting constant for DMPO-O_2H (αN = 13.8 G; $\alpha H(\beta)$ = 11.1 G; $\alpha H(\gamma)$ = 1.2 G) [46]. In contrast, no obvious DMPO–OH signals could be detected in the dark or even under VL irradiation, revealing that no ·OH was produced in this photocatalytic system (Fig. 10b). In conclusion, ESR technique confirms that $O_2^{\cdot-}$ rather than ·OH is the major ROS responsible for the photodecomposition of RhB.

Besides determining the ROS, the scavenging experiments were conducted to further illustrate the photocatalytic mechanism [47,48]. As displayed in Fig. 11, IPA (1 mmol), BQ (0.05 mmol) or AO (1 mmol) were used to quench ·OH, $O_2^{\cdot-}$ or h^+ species in the RhB degradation, respectively. The degradation rate of RhB by using 0.4WB in 90 min of reaction was 100% without any scavengers. When IPA was introduced, the degradation rate of RhB slightly declined, implying that ·OH plays a minor role in RhB degradation. Comparatively, the addition of BQ or AO significantly inhibited RhB removal, highlighting that $O_2^{\cdot-}$ and h^+ species are both effective in the photodegradation process over WO_3/Bi_2MoO_6. It can be concluded that $O_2^{\cdot-}$ and h^+ radicals are crucial species involved in the pollutant degradation over WO_3/Bi_2MoO_6 while ·OH plays a subordinate role, as verified by the trapping experiments and ESR analysis.

To unveil whether the direct contact is prerequisite for the photo-degradation of RhB over WO_3/Bi_2MoO_6, a reactor equipped with the separation system (Fig. 12a) was designed and set up according to the reported literature [49,50]. Briefly, the separation system composed of a dialysis bag that allows the free entry of small molecules (*e.g.*, ions, reactive species) but no entry of photocatalysts and slight leakage of RhB dye. In this system, aqueous RhB solution (20 mg/L, 20 mL) was poured into the dialysis bag, which was suspended in 300 mL of water in the presence or absence of 0.4WB. Fig. 12b presents the percentages of RhB in the inner system or outer system under different conditions. The control experiment shows that 78.4% of RhB remains in the dialysis bag and 21.6% of RhB leaks into the outer system within 90 min of VL irradiation, due to the nature of semipermeable membrane. When the 0.4WB catalyst was added into the outer system and exposed to VL for 90 min, the concentration of RhB inside the dialysis bag did not apparently change as compared to the control system, implying that most of the active species do not pass through the membrane to participate in the degradation of RhB. By contrast, no RhB can be

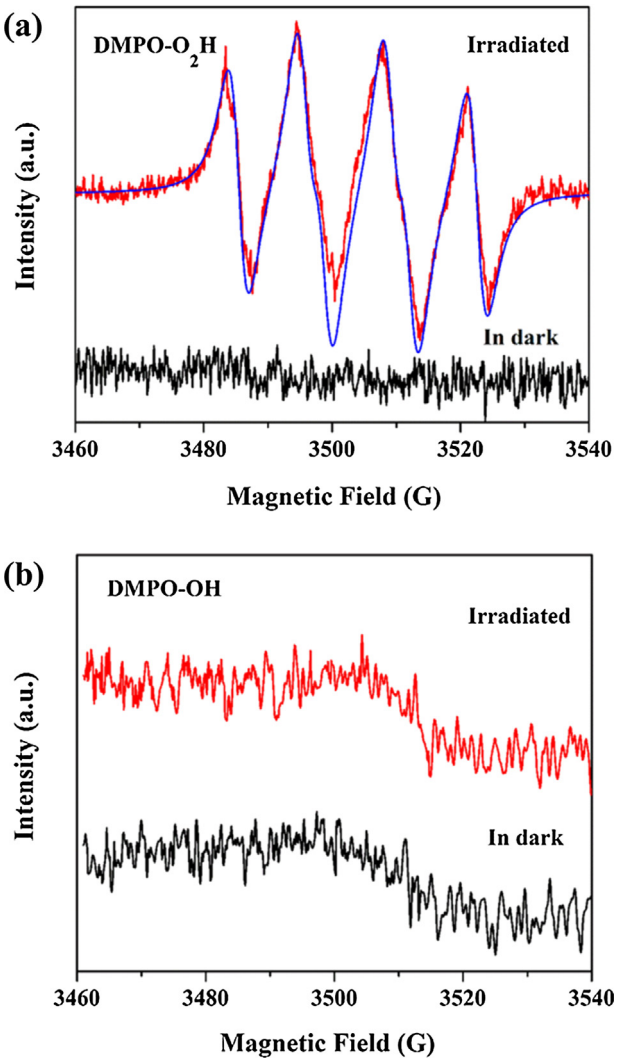

Fig. 10. ESR spectra of 0.4BW for DMPO-O_2H (a) and DMPO-OH (b). The spectra in red and blue in figure a denote experimental and simulated data, respectively. (For interpretation of the references to color in this figure legend, the reader is referred to the web version of this article.)

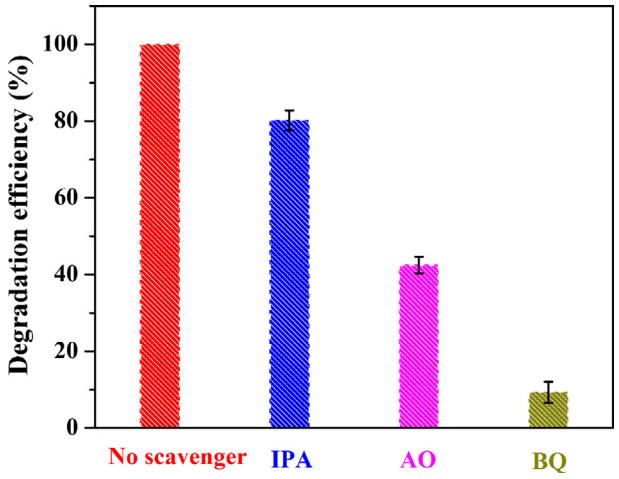

Fig. 11. Effects of various quenchers on RhB degradation performance by using 0.4WB.

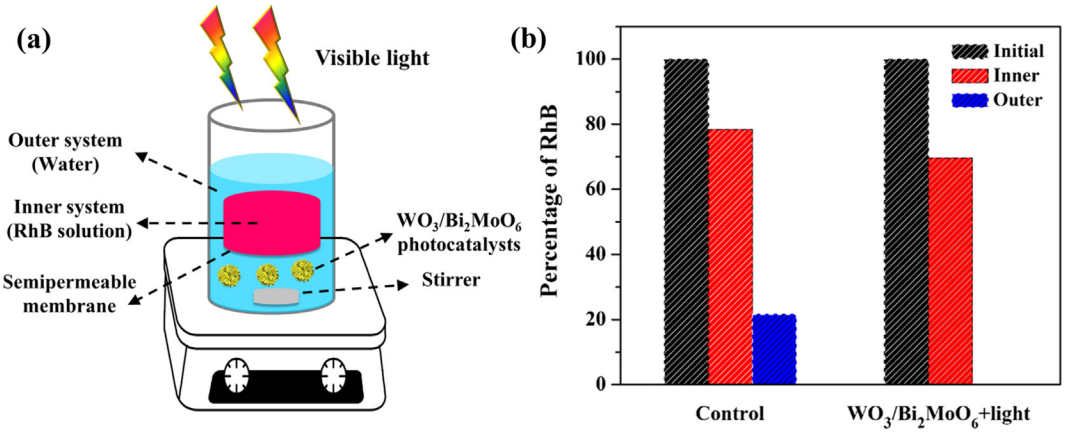

Fig. 12. (a) Schematic illustration of the reactor equipped with the separation system, (b) Percentages of RhB inside and outside a semipermeable membrane container when the outer system is under different conditions.

detected outside the dialysis bag, reflecting that the diffused RhB is first adsorbed on the surface of 0.4WB and then photocatalytically decomposed by the photo-generated reactive species. This experiment clearly verifies that the direct contact between 0.4WB and contaminants is the prerequisite for the photocatalysis.

For further determining the transfer pathway of photo-excited electrons and holes, the band edge potentials of pure Bi_2MoO_6, and WO_3 were tested by UV–vis DRS and the VB-XPS spectra (Fig. 13). The band gap energies of Bi_2MoO_6 and WO_3 were estimated from the UV–vis DRS by using the kubelka-Munk function: $\alpha hv = A(hv\text{-}Eg)^{n/2}$, where Eg, α, ν, and A separately represents band gap, absorption coefficient, light frequency, and a constant [51]. n equals to 1 or 4 for direct or indirect band-gap semiconductor. n equals to 4 for Bi_2MoO_6 [18] and WO_3 [51]. Fig. 13a presents the plot of $(\alpha hv)^{1/2}$ versus hv. The Eg values of Bi_2MoO_6 and WO_3 are counted as 2.66 and 2.76 eV, respectively. The valence band (VB) values of Bi_2MoO_6 and WO_3 were measured to be 2.34 and 3.32 eV (versus NHE) (Fig. 13b). Accordingly, the conduction band (CB) values of Bi_2MoO_6 and WO_3 were calculated to be −0.32 and 0.56 eV. Based on the alignment of their band edge potentials, the transfer path of photo-excited carriers at the interface are depicted in Fig. 14.

According to these experimental results and discussion, the photocatalytic pollutant degradation mechanism is proposed (Fig. 14). With VL illumination, both Bi_2MoO_6 and WO_3 can be driven synchronously to produce charge carriers. In terms of the fact that the CB or VB edge potential of Bi_2MoO_6 is much more positive than that of WO_3, the photo-excited electrons on the CB of Bi_2MoO_6 can readily move to that of WO_3, resulting the accumulation of electrons on WO_3. Subsequently, these electrons are consumed by reducing O_2 for the generation of reactive $O_2^{\cdot-}$ species. Simultaneously generated holes on the VB of WO_3 can be injected into that of Bi_2MoO_6, resulting the accumulation of holes on Bi_2MoO_6. In such a special hetero-structure, the preferential transfer of photo-generated carriers greatly enhances the electron-hole separation efficiency, as well as pronouncedly upgrades the photocatalytic property [3,32]. Eventually, the pollutant degradation and mineralization was achieved under the attack of reactive $O_2^{\cdot-}$ species and h^+, as confirmed by trapping experiments and ESR tests (Figs. 10 and 11). It is indisputable that the component synergy in the unique WO_3/Bi_2MoO_6 hetero-structure plays the key roles in its enhanced VL utilization, efficient carrier separation, and the resulting excellent photocatalytic performance in the removal of toxic contaminants.

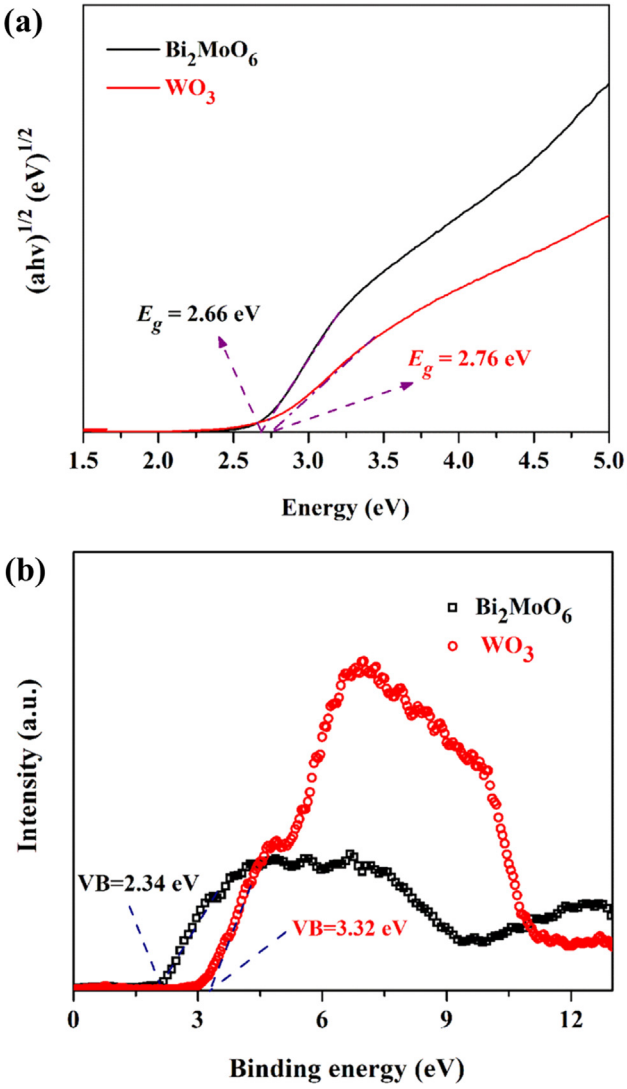

Fig. 13. (a) Tauc's plots of Bi_2MoO_6, and WO_3; (b) VB XPS spectra of Bi_2MoO_6 and WO_3.

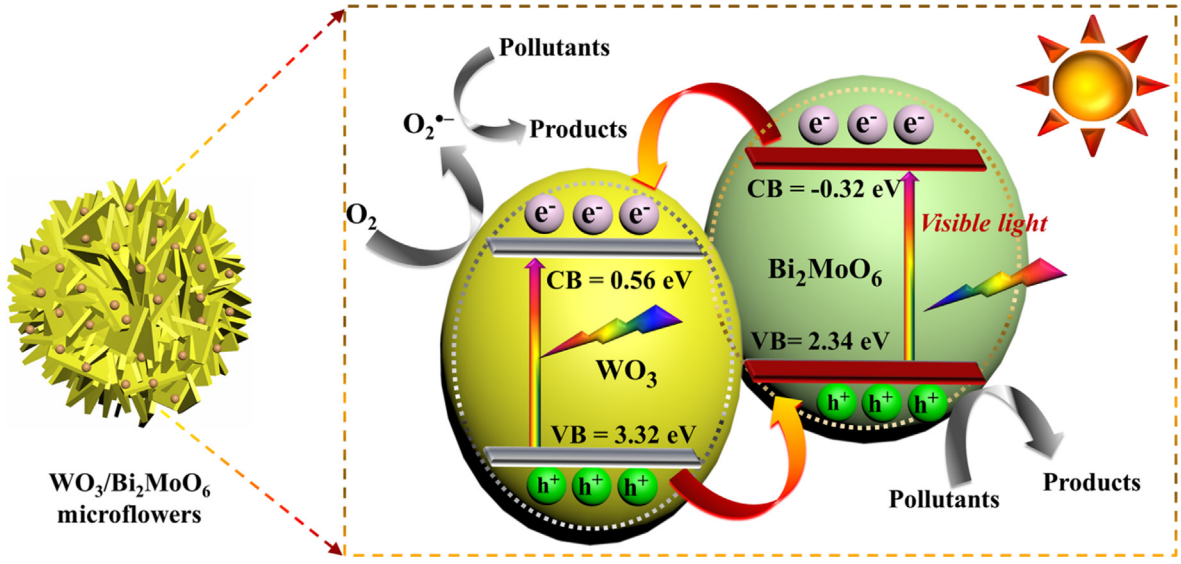

Fig. 14. Proposed photocatalysis mechanism of WO_3/Bi_2MoO_6 toward refractory contaminants under VL.

4. Conclusions

In summary, hierarchical WO_3/Bi_2MoO_6 heterojunctions with closely interfacial interactions were fabricated via an achievable electrospinning–calcination–solvothermal approach. The photocatalytic degradation of RhB and TC were conducted on WO_3/Bi_2MoO_6 heterojunctions under VL. The photocatalytic activities of WO_3/Bi_2MoO_6 were markedly improved in contrast with pure WO_3 and Bi_2MoO_6. When the WO_3/Bi_2MoO_6 molar ratio reaches 0.4/1.0, the 0.4WB possesses the maximum photocatalytic activity among all samples. It is proposed that the component synergy in the unique WO_3/Bi_2MoO_6 heterostructure endows the catalyst with enhanced VL utilization, and effective carrier separation, which further results in an excellent photocatalytic performance. The scavenging experiments and ESR analysis indicate that the main radicals involved in the pollutant degradation are O_2^- and h^+ species. It is worthy of noting that the direct contact between WO_3/Bi_2MoO_6 and contaminant is prerequisite for the photodegradation of pollutants. Additionally, the cycling tests and TOC analysis verify that 0.4WB is a kind of stable catalyst with satisfactory mineralization capability. Thus, this study provides an effective way to construct highly efficient and stable VLD heterojunction photocatalysts for practical environmental remediation.

Acknowledgments

This work has been financially supported by the Fundamental Research Funds for Zhejiang Provincial Universities and Research Institutes (2019JZ00009), the National Natural Science Foundation of China (51708504 and 51602049), the Public Projects of Zhejiang Province (LGN18E080003), the Science and Technology Project of Zhoushan (2017C41006), and the China Postdoctoral Science Foundation (2017M610217, 2018T110322).

Appendix A. Supplementary material

Supplementary data to this article can be found online at https://doi.org/10.1016/j.jcis.2019.08.077.

References

[1] M.-Q. Yang, M. Gao, M. Hong, G.W. Ho, Adv. Mater. 30 (2018) 1802894.
[2] P. Singh, A. Borthakur, J. Clean. Prod. 196 (2018) 1669–1680.
[3] S.S. Zhu, D.W. Wang, Adv. Energy Mater. 7 (2017) 1700841.
[4] G. Zhang, G. Li, T. Heil, S. Zafeiratos, A. Savateev, X. Wang, M. Antonietti, Angew. Chem. 58 (2019) 3433–3437.
[5] F. Pulizzi, W. Sun, Nat. Nanotechnol. 13 (2018) 633.
[6] M. Pirhashemi, A. Habibi-Yangjeh, S.R. Pouran, J. Ind. Eng. Chem. 62 (2018) 1–25.
[7] F. Chang, F. Wu, J. Zheng, W. Cheng, W. Yan, B. Deng, X. Hu, Chemosphere 210 (2018) 257–266.
[8] Y. Liu, G.Q. Zhu, J.Z. Gao, R.L. Zhu, M. Hojamberdiev, C.H. Wang, X.M. Wei, P. Liu, Appl. Catal. B 205 (2017) 421–432.
[9] S. Singh, R. Sharm, Sol. Energy Mater. Sol. Cells 186 (2018) 208–216.
[10] A. Prakash, M. Dan, S. Yu, S. Wei, Y. Li, F. Wang, Y. Zhou, Sol. Energy Mater. Sol. Cells 180 (2018) 205–212.
[11] M.Z. Ghori, S. Veziroglu, B. Henkel, A. Vahl, O. Polonskyi, T. Strunskus, F. Faupel, O.C. Aktas, Sol. Energy Mater. Sol. Cells 178 (2018) 170–178.
[12] G. Giannakakis, M. Flytzani-Stephanopoulos, E.C.H. Sykes, Acc. Chem. Res. 52 (2019) 237–247.
[13] L. Zhang, C. Lin, D. Zhang, L. Gong, Y. Zhu, Q. Xu, H. Li, Z. Xia, Adv. Mater. 31 (2019) 1805252.
[14] S. Li, J. Chen, Y. Liu, K. Xu, J. Liu, J. Alloy. Compd. 781 (2019) 582–588.
[15] S. Li, J. Chen, W. Jiang, Y. Liu, Y. Ge, J. Liu, J. Colloid Interface Sci. 548 (2019) 12–19.
[16] R. He, D. Xu, B. Cheng, J. Yu, W. Ho, Nanoscale Horiz. 3 (2018) 464–504.
[17] H. Yu, L. Jiang, H. Wang, B. Huang, X. Yuan, J. Huang, J. Zhang, G. Zeng, Small 15 (2019) 1901008.
[18] Y. Hao, X. Dong, S. Zhai, X. Wang, H. Ma, X. Zhang, Chem. Commun. 52 (2016) 6525–6528.
[19] S. Li, X. Shen, J. Liu, L. Zhang, Environ. Sci. NANO 4 (2017) 1155–1167.
[20] F. Mei, J. Zhang, K. Dai, G. Zhu, C. Liang, Dalton Trans. 48 (2019) 1067–1074.
[21] K. Jing, W. Ma, Y. Ren, J. Xiong, B. Guo, Y. Song, S. Liang, L. Wu, Appl. Catal. B 243 (2019) 10–18.
[22] X. Meng, Z. Zhang, Appl. Catal. B 209 (2017) 383–393.
[23] Y. Zhong, Z. He, D. Chen, W. Hao, Appl. Surf. Sci. 467–468 (2019) 740–748.
[24] J. Di, X. Zhao, C. Lian, M. Ji, J. Xia, J. Xiong, W. Zhou, X. Cao, Y. She, H. Liu, K.P. Loh, S.J. Pennycook, H. Li, Z. Liu, Nano Energy 61 (2019) 54–59.
[25] Y. Wu, M. Song, Z. Chai, X. Wang, Inorg. Chem. 58 (2019) 7374–7384.
[26] J.L. Zhang, Z. Ma, J. Taiwan Inst. Chem. Eng. 71 (2018) 156–164.
[27] Q.Q. Meng, Y.S. Zhou, G. Chen, Y.D. Hu, C. Lv, L.S. Qiang, W.N. Xing, Chem. Eng. J. 334 (2018) 334–343.
[28] R. Tao, C. Shao, X. Li, Y.C. Liu, J. Colloid Interface Sci. 529 (2018) 404–414.
[29] S. Li, S. Hu, W. Jiang, Y. Zhou, J. Liu, Z. Wang, J. Colloid Interface Sci. 530 (2018) 171–178.
[30] S. Li, S. Hu, W. Jiang, Y. Liu, Y. Zhou, Y. Liu, L. Mo, J. Colloid Interface Sci. 521 (2018) 42–49.
[31] S. Li, S. Hu, J. Zhang, W. Jiang, J. Liu, J. Colloid Interface Sci. 497 (2017) 93–101.
[32] H.L. Wang, L.S. Zhang, Z.G. Chen, J.Q. Hu, S.J. Li, Z.H. Wang, J.S. Liu, X.C. Wang, Chem. Soci. Rev. 43 (2014) 5234–5244.
[33] T. Xiao, Z. Tang, Y. Yang, L. Tang, Y. Zhou, Z. Zou, Appl. Catal. B 220 (2018) 417–428.
[34] E. Grilla, A. Petala, Z. Frontistis, I.K. Konstantinou, D.I. Kondarides, D. Mantzavinos, Appl. Catal. B 231 (2018) 73–81.
[35] J. Zhang, Y. Guo, Y. Xiong, D. Zhou, S. Dong, J. Catal. 356 (2017) 1–13.
[36] X.D. Ma, W.X. Ma, D.L. Jiang, D. Li, S.C. Meng, M. Chen, J. Colloid Interface Sci. 506 (2017) 93–101.

[37] J.L. Zhang, L.S. Zhang, X.F. Shen, P.F. Xu, J.S. Liu, CrystEngComm 18 (2016) 3856–3865.
[38] S. Li, W. Jiang, S. Hu, Y. Liu, Y. Liu, K. Xu, J. Liu, Beilstein J. Nanotechnol. 9 (2018) 2297–2305.
[39] J. Zheng, F. Chang, M. Jiao, Q. Xu, B. Deng, X. Hu, J. Colloid Interface Sci. 510 (2018) 20–31.
[40] S. Li, S. Hu, W. Jiang, Y. Liu, J. Liu, Z. Wang, J. Colloid Interface Sci. 501 (2017) 156–163.
[41] S. Li, S. Hu, W. Jiang, Y. Liu, J. Liu, Z. Wang, Molecular Catalysis 435 (2017) 135–143.
[42] F. Chang, X. Wang, J. Luo, J. Wang, Y. Xie, B. Deng, X. Hu, J. Mol. Catal. A: Chem. 427 (2017) 45–53.
[43] F. Chang, J. Zheng, X. Wang, Q. Xua, B. Deng, X. Hu, X. Liu, Mat. Sci. Semicon. Proc. 75 (2018) 183–192.
[44] X. Xin, S.-H. Li, N. Zhang, Z.-R. Tang, Y.-J. Xu, Appl. Catal. B 245 (2019) 343–350.
[45] Z.H. Wang, W.H. Ma, C.C. Chen, H.W. Ji, J.C. Zhao, Chem. Eng. J. 170 (2011) 353–362.
[46] F.A. Villamena, Reactive Species Detection in Biology: From Fluorescence to Electron Paramagnetic Resonance Spectroscopy, Elsevier, 2016.
[47] S. Li, S. Hu, K. Xu, W. Jiang, Y. Liu, Z. Leng, J. Liu, J. Colloid Interface Sci. 504 (2017) 561–569.
[48] Y. Wang, H. Wang, A. Xu, Z. Song, J. Mater. Sci.: Mater. Electron. 29 (2018) 16691–16701.
[49] L.-S. Zhang, K.-H. Wong, D.-Q. Zhang, C. Hu, J.C. Yu, C.-Y. Chan, P.-K. Wong, Environ. Sci. Technol. 43 (2009) 7883–7888.
[50] X. Shen, T. Zhang, P. Xu, L. Zhang, J. Liu, Z. Chen, Appl. Catal. B 219 (2017) 425–431.
[51] H. Zhou, Z. Wen, J. Liu, K. Ke, D. Xiaogang, S. Wang, Appl. Catal. B 242 (2019) 76–84.